Aggregate

WILEY

Aggregate

RESEARCH ARTICLE OPEN ACCESS

Magnetic-Field-Driven Precision Fabrication of Multifunctional Microgels for Biomedical Applications

Yingying Hou[1] | Huaibin Wang[1,2] | Long Chen[1] | Kangrui Yuan[3] | Jianhua Qiu[1] | Lijie Chen[1] | Bingbing Zhan[1] | Zeqing Li[1] | Lingran Du[1] | Maobin Xie[4] | Zeyu Luo[5] | Yongqing He[6] | Guosheng Tang[1,7]

[1]Guangzhou Municipal and Guangdong Provincial Key Laboratory of Molecular Target and Clinical Pharmacology, the NMPA and State Key Laboratory of Respiratory Disease, School of Pharmaceutical Sciences and the Fifth Affiliated Hospital, Guangzhou Medical University, Guangzhou, China | [2]Department of Epidemiology and Biostatistics, School of Public Health, Guangdong Medical University, Zhanjiang, China | [3]National Key Laboratory for the Development and Utilization of Forest Food Resources, Joint Laboratory of Advanced Biomedical Materials (NFU-UGent), Jiangsu Co-Innovation Center of Efficient Processing and Utilization of Forest Resources, Nanjing Forestry University, Nanjing, China | [4]The Fourth Affiliated Hospital of Guangzhou Medical University, School of Biomedical Engineering, Guangzhou Medical University, Guangzhou, China | [5]Department of Orthopaedics, Orthopaedic Research Institute, West China Hospital, Sichuan University, Chengdu, China | [6]Department of Energy and Environment, Southeast University, Nanjing, China | [7]Key Laboratory of Bioactive Materials, Ministry of Education, Nankai University, Tianjin, China

Correspondence: Zeyu Luo (luozy@wchscu.edu.cn) | Yongqing He (yqhe@seu.edu.cn) | Guosheng Tang (guoshengtang@gzhmu.edu.cn)

Received: 20 January 2026 | **Revised:** 17 March 2026 | **Accepted:** 5 May 2026

Keywords: hemodialysis | magnetic field | microgels | SPIONs | vascular embolism

ABSTRACT

The fabrication of monodisperse microgels has achieved considerable success and has transformed many fields. However, conventional methods typically rely on external shear forces, interfacial perturbations, or toxic solvents, which restrict their application flexibility. This study presents a novel magnetic-field-actuated strategy for fabricating uniform microgels (300–900 μm) with tunable morphologies, including microspheres and microfibers, bypassing the need for external shear forces, interfacial perturbations, or toxic solvents. By integrating superparamagnetic iron oxide nanoparticles (SPIONs) into hydrogel precursors, internal magnetic stress gradients induce self-driven droplet segmentation, enabling precise control over particle size and structure with high-throughput production and exceptional uniformity. These biocompatible microgels exhibit robust magnetic responsiveness, facilitating precise positioning and occlusion in vascular embolism models and enhancing toxin clearance in hemodialysis by three to four times through turbulence induced by magnetically driven rotation. This magnetically programmable platform merges microgel synthesis and functionalization, offering a versatile class of carriers with adaptable structures for regenerative medicine and precision medicine applications.

1 | Introduction

Microgels, three-dimensional cross-linked hydrophilic networks, have transformed biomedical engineering and adaptive material design with their tunable mechanics and biocompatible structures [1, 2]. Microfluidic techniques produce monodisperse droplets (microliters to femtoliters) using flow-focusing or droplet-breakup methods, widely studied for microgel fabrication due to their precise control over particle morphology and complexity [3–8]. Microgel fabrication in microfluidics involves two key steps: segmenting hydrogel precursors into discrete microdomains [9] and consolidating them through cross-linking [10]. Typically, external energy fields, such as oil-phase shear forces, destabilize precursor interfaces to form droplets [4, 11].

Yingying Hou, Huaibin Wang, and Long Chen contributed equally to this work.

This is an open access article under the terms of the Creative Commons Attribution License, which permits use, distribution and reproduction in any medium, provided the original work is properly cited.
© 2026 The Author(s). *Aggregate* published by SCUT, AIEI, and John Wiley & Sons Australia, Ltd.

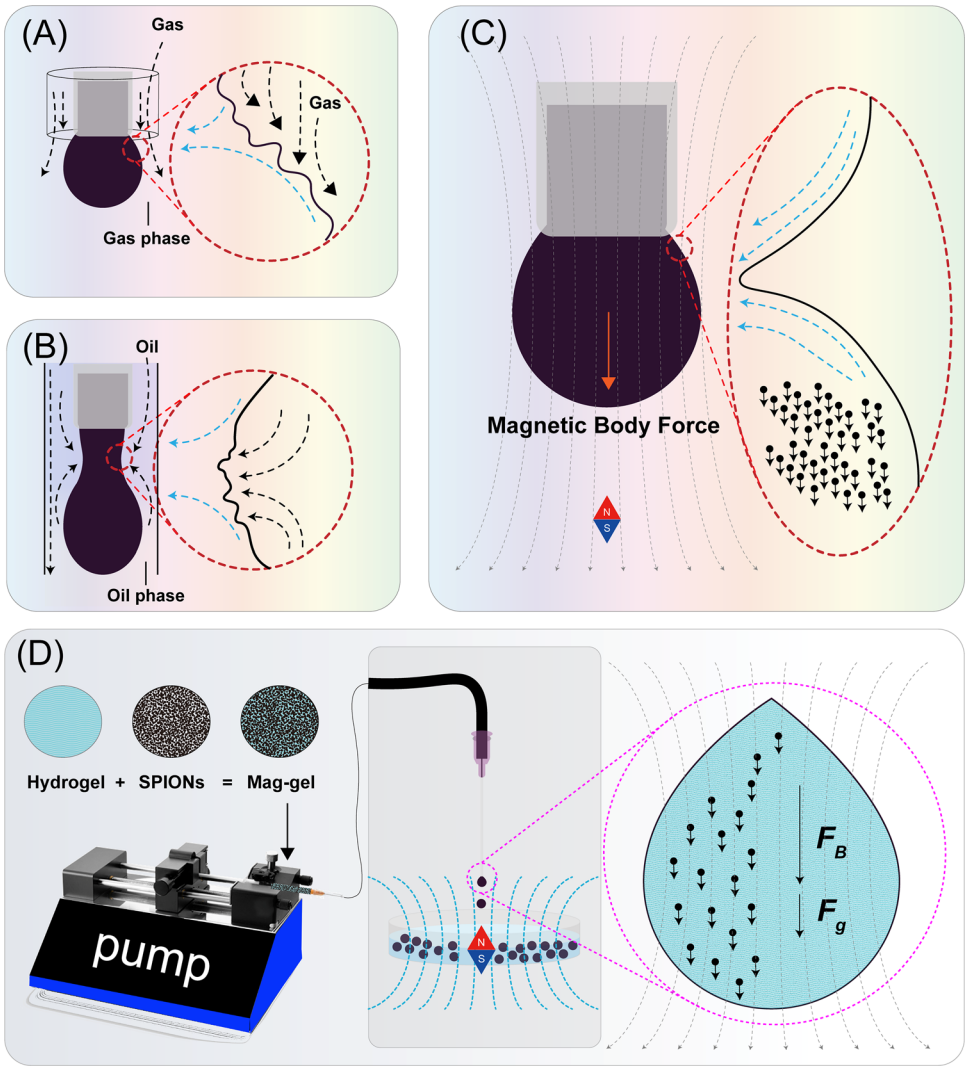

FIGURE 1 | Microgel fabrication through intrinsic magnetic stress-driven fragmentation. (A) Schematic illustrating interfacial instability induced by external shear forces (black-dashed arrows) under gas phase and (B) oil phase. Turbulent shear generates hydrodynamic stress (blue arrows). External shear forces and hydrodynamic stress are abstractly represented. (C) Schematic of magnetization-driven: the magnetization of SPIONs under external fields generates body forces oriented parallel to field lines, causing progressive droplet elongation. The resultant strain energy localization drives necking rupture. (D) Schematic of the digitally controlled syringe pump, which extrudes a precursor solution through a nozzle above a magnetic array. Combined magnetic stress (F_B) and gravity (F_g) synergistically induce external shear-free necking rupture. Detached droplets solidify in a cross-linking bath, preserving payload integrity while enabling tunable architecture.

This approach requires the fabrication of complex microfluidic devices and specialized equipment, which increases costs and limits industrial scalability. While these methods improve scalability, their reliance on external mechanical or fluidic forces can damage encapsulated biologics due to turbulent shear (Figure 1A,B). Alternative approaches, like centrifugation-based methods and in-air microfluidics, have been explored to address these issues for broader biomedical applications. Nonetheless, all current techniques depend on external forces to overcome the precursor's surface tension (γ) [12], governed by the Laplace pressure criterion ($\Delta P = 2\gamma/R$) [13, 14], limiting spatiotemporal control and complicating process intensification.

Recent advancements have focused on intrinsic force engineering to overcome these limitations, by incorporating responsive actuators into precursors for self-regulated segmentation [15, 16]. Superparamagnetic iron oxide nanoparticles (SPIONs) offer a robust platform for intrinsic actuation [17]. Their single-domain magnetism facilitates field-programmable stress via Néel relaxation-driven magnetophoresis, converting magnetic field gradients into localized mechanical work [18]. When dispersed in hydrogel precursors, SPIONs generate internal stress gradients under non-uniform magnetic fields, enabling a self-segmentation process that contactlessly tunes microgel sizes (300–900 μm) by varying field strength (Figure 1C). This approach can be extended to produce anisotropic microgels and microfibers with tailored architectures. Moreover, the retained SPIONs endow microgels with multifunctionality, including magnetothermal responsiveness and magnetic motion [19, 20].

Transitioning from external force-driven methods to intrinsically self-actuating approaches marks a breakthrough in microgel

26924560, 2026, 5, Downloaded from https://onlinelibrary.wiley.com/doi/10.1002/agt2.70365 by Guosheng Tang - Nanjing Forestry University , Wiley Online Library on [20/05/2026]. See the Terms and Conditions (https://onlinelibrary.wiley.com/terms-and-conditions) on Wiley Online Library for rules of use; OA articles are governed by the applicable Creative Commons License

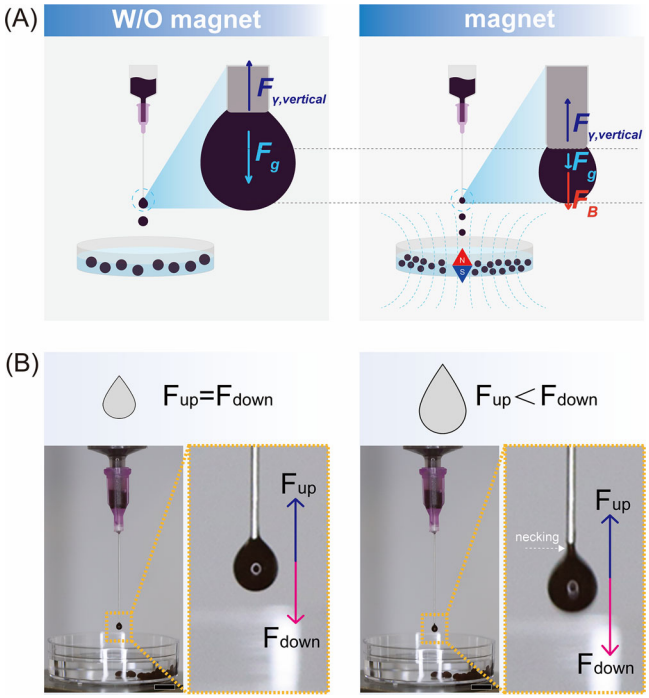

FIGURE 2 | Schematic of magnetic-field-modulated droplet detachment. (A) Schematic illustration of gravity-only detachment requires large droplets ($F_g > F_{\gamma,vertical}$) (left). Magnetic force (F_B) reduces the critical volume (right). (B) Photographs showing force balance evolution: initial equilibrium ($F_{up} = F_{down}$) shifts to detachment when $F_{down} > F_{up}$.

fabrication. By embedding SPIONs in the precursor matrix, this study introduces a magnetic-field-controlled strategy for droplet/structure segmentation and magnetically programmable dynamic behavior (Figure 1D). This approach eliminates shear-induced damage to biologics that can occur in microfluidics, ensuring payload integrity. It enables real-time tuning of microgel size and architecture by programming magnetic field gradients. SPIONs impart multifunctional capabilities, including magnetic actuation, magnetothermal response, and spatial control [21]. The method's potential was validated in key biomedical applications: microgels navigated 3D-printed microfluidic mazes with precise magnetic guidance, achieved targeted embolization in an in vitro Tesla valve model for minimally invasive therapies, and enhanced clearance rates in a dialysis model through magnetically induced rotation. This integration of biocompatible, shear-free fabrication and multifunctionality paves the way for advanced microgels in precision medicine and adaptive materials, offering unmatched structural precision and responsive functionality.

2 | Results and Discussions

2.1 | Magnetically Actuated Droplet Detachment Dynamics

This study introduces a magnetic-field-driven strategy to overcome the limitations of traditional microgel fabrication, which relies on gravity to form droplets larger than 1000 μm (Figure 2A). By embedding SPIONs in hydrogel precursors, magnetic forces enable precise control over droplet size and uniformity, reducing reliance on external shear or large volumes. This approach aims to achieve monodisperse microgels with tunable diameters, thereby enhancing scalability and precision. To evaluate the method's feasibility, the force balance governing droplet detachment was assessed. This balance involves gravitational, magnetic, and surface tension forces, with the gravitational force for a spherical droplet given by [22]:

$$F_g = \rho g V = \frac{4}{3}\pi\rho g R^3 \tag{1}$$

where ρ is the fluid density, $V = 4/3\pi R^3$ is the droplet volume, $g = 9.81\ m/s^2$ is gravitational acceleration, and R is the droplet radius. The magnetic force arises from SPIONs under a nonuniform magnetic field H, with linear magnetization $M = \chi H$ [23]:

$$F_B = \frac{1}{2}\mu_0 \chi V \frac{\partial H^2}{\partial z} = \frac{2}{3}\pi\mu_0\chi R^3 \frac{\partial H^2}{\partial z} \tag{2}$$

where $\mu_0 = 4\pi \times 10^{-7}$ H/m is the vacuum permeability, χ is the magnetic susceptibility, and $\partial H^2/\partial z$ is the axial field gradient. Both forces scale with R^3, enabling smaller droplets under magnetic-field-driven conditions. Surface tension resists detachment [22]:

$$F_{\gamma,vertical} = \pi D\gamma \sin\theta \tag{3}$$

where D is the nozzle diameter, γ is the surface tension of the alginate-SPION mixture, and θ is the contact angle, influenced by droplet shape (predicted by [24, 25], with a deformation ratio of ~1 without magnetic fields [26]). Magnetic fields adjust γ slightly, as detailed in Eq. S5.

Simulated force–radius curves (Figure S1) show the total downward force ($F_{down} = F_g + F_B$) versus the maximum surface tension force ($F_{\gamma,MAX}$). In the quasi-static growth phase, $F_{down} \le F_{\gamma,MAX}$, and the droplet grows until reaching the critical radius R_{crit}. In the instability-driven detachment phase, $F_{down} > F_{\gamma,MAX}$, triggering detachment:

$$R_{crit} = \left(\frac{3F_{\gamma,MAX}}{4\pi(\rho g + \frac{1}{2}\mu_0\chi\partial H^2/\partial z)}\right)^{1/3} \tag{4}$$

This model, validated by simulations, demonstrates that magnetic-field-driven reduction of R_{crit} enables precise microgel fabrication (Figure 2B) [23].

2.2 | Magnetically Actuated Microgel Fabrication

To assess the system's broad applicability following theoretical analysis, an extrusion setup was employed, using a syringe pump to deliver a SPION-sodium alginate (Na-Alg) precursor through tubing to a nozzle. Upon application of a magnetic field, the droplet promptly detached at the nozzle tip, with droplets rapidly cross-linking into Ca-Alg microspheres in an aqueous $CaCl_2$ bath. The syringe, loaded with Na-Alg solution containing SPIONs, was connected to the nozzle. Varying the Na-Alg extrusion speed revealed its impact on microgel formation: low speeds produced discrete microspheres, while higher speeds

26924560, 2026, 5, Downloaded from https://onlinelibrary.wiley.com/doi/10.1002/agt2.70365 by Guosheng Tang - Nanjing Forestry University , Wiley Online Library on [20/05/2026]. See the Terms and Conditions (https://onlinelibrary.wiley.com/terms-and-conditions) on Wiley Online Library for rules of use; OA articles are governed by the applicable Creative Commons License

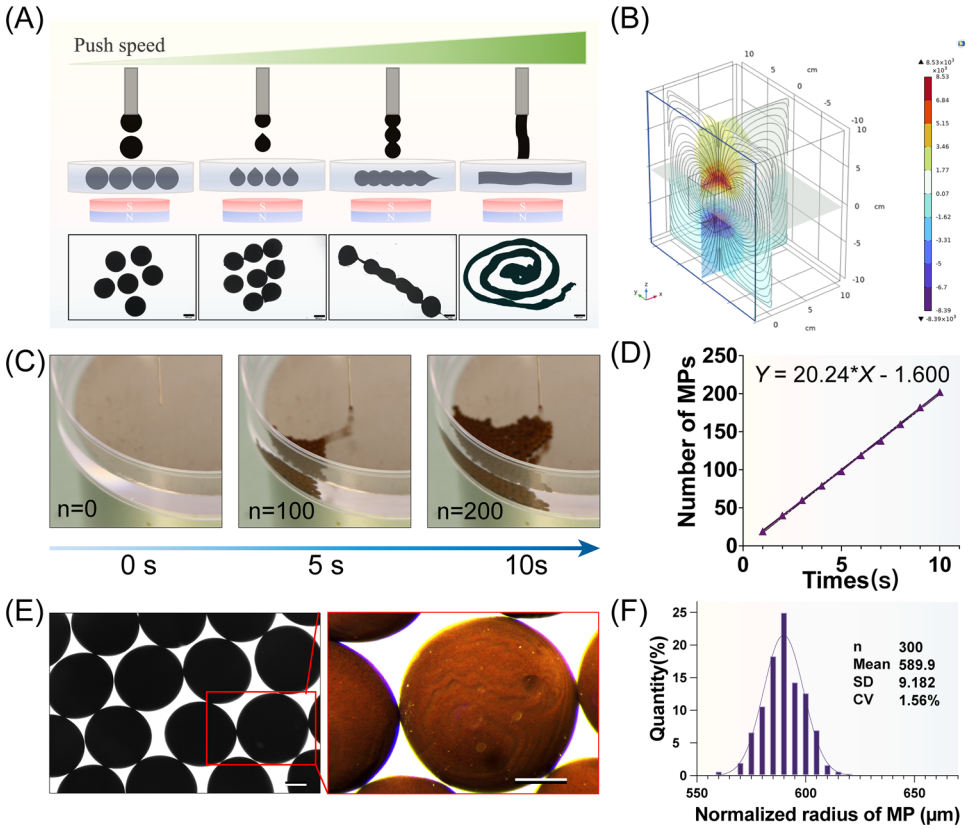

FIGURE 3 | Morphological evolution and characterization of magnetically assisted microgel fabrication. (A) Schematic illustration and experimental results of microgel formation at different extrusion speeds: isolated microspheres at low speeds, droplet-shaped particles with tails at intermediate speeds, bead-like structures from overlapping droplets, and continuous microfibers at high speeds, scale bars: 200 μm. (B) Simulation of magnetic flux density distribution near a block magnet, showing non-linear decay with increasing distance. (C) Photographs showing the fabrication of microgels at various time points, and (D) corresponding quantitative analyses of production quantity (*Y*-axis) versus fabrication duration (*X*-axis). (E) Photographs showing the microspherical microgels with uniform size and shape, arranged in ordered alignment under standard illumination (left), reddish-brown coloration of the same microgels under intense directional light (right), scale bars: 200 μm. (F) Size distribution histogram of microgels (MP, microparticles), $n = 300$.

caused faster droplet descent, solidifying into droplet-shaped particles with small tails. Further speed increases led to overlapping droplets, forming bead-like structures interspersed with continuous droplets. Above a critical speed threshold, the system transitioned from discrete spherical microgels to continuous microfibers (Figure 3A).

The magnetic flux density decreases non-linearly with distance from the magnet, showing significantly higher intensity in proximal regions than distal ones (Figure 3B and Figure S2). Placing the magnet closer accelerates microgel fabrication, enabling rapid production in short timeframes (Figure 3C and Videos S1 and S2). The production rate is consistently controlled, achieving approximately 20 microgels/s (Figure 3D). For comparison, Shao et al. reported a microfluidic fabrication platform that generated 7–18 hydrogel microspheres every 3 s (≈2–6 microspheres/s) at the selected flow ratio [27]. More broadly, representative microfluidic microgel/microsphere fabrication studies have reported throughputs on the order of a few particles per second) [28, 29], suggesting that our magnetic-driven approach offers a competitive advantage in microgel fabrication efficiency and throughput. Moreover, the resulting microgels display high uniformity, with a reddish-brown hue under intense illumination due to the incorporation of SPIONs (Figure 3E), and exhibit very low polydispersity (Figure 3F).

2.3 | Fabrication of Size-Tunable Spherical Microgels

Systematic analysis of magnetic flux density and interfacial tension dynamics elucidated key mechanisms for controlling microsphere dimensions. Finite-element simulations of a block magnet's spatial magnetic flux distribution revealed an inverse relationship between magnetic flux density (B) and vertical Z-axis displacement (Figure 4A). To improve reproducibility, we additionally quantified the absolute magnetic flux density (B) and its axial spatial gradient (dB/dz) at the nozzle for each separation distance (z) used in droplet generation (Figure S4). These measurements, supported by numerical simulation, establish a direct mapping between z and the local magnetic conditions governing droplet breakup. At a distance of 0.2 cm from the magnet surface, the peripheral magnetic flux density was approximately 20% stronger than at the center (Figure 4B), highlighting edge-enhanced field properties critical for droplet manipulation.

26924560, 2026, 5, Downloaded from https://onlinelibrary.wiley.com/doi/10.1002/agt2.70365 by Guosheng Tang - Nanjing Forestry University , Wiley Online Library on [20/05/2026]. See the Terms and Conditions (https://onlinelibrary.wiley.com/terms-and-conditions) on Wiley Online Library for rules of use; OA articles are governed by the applicable Creative Commons License

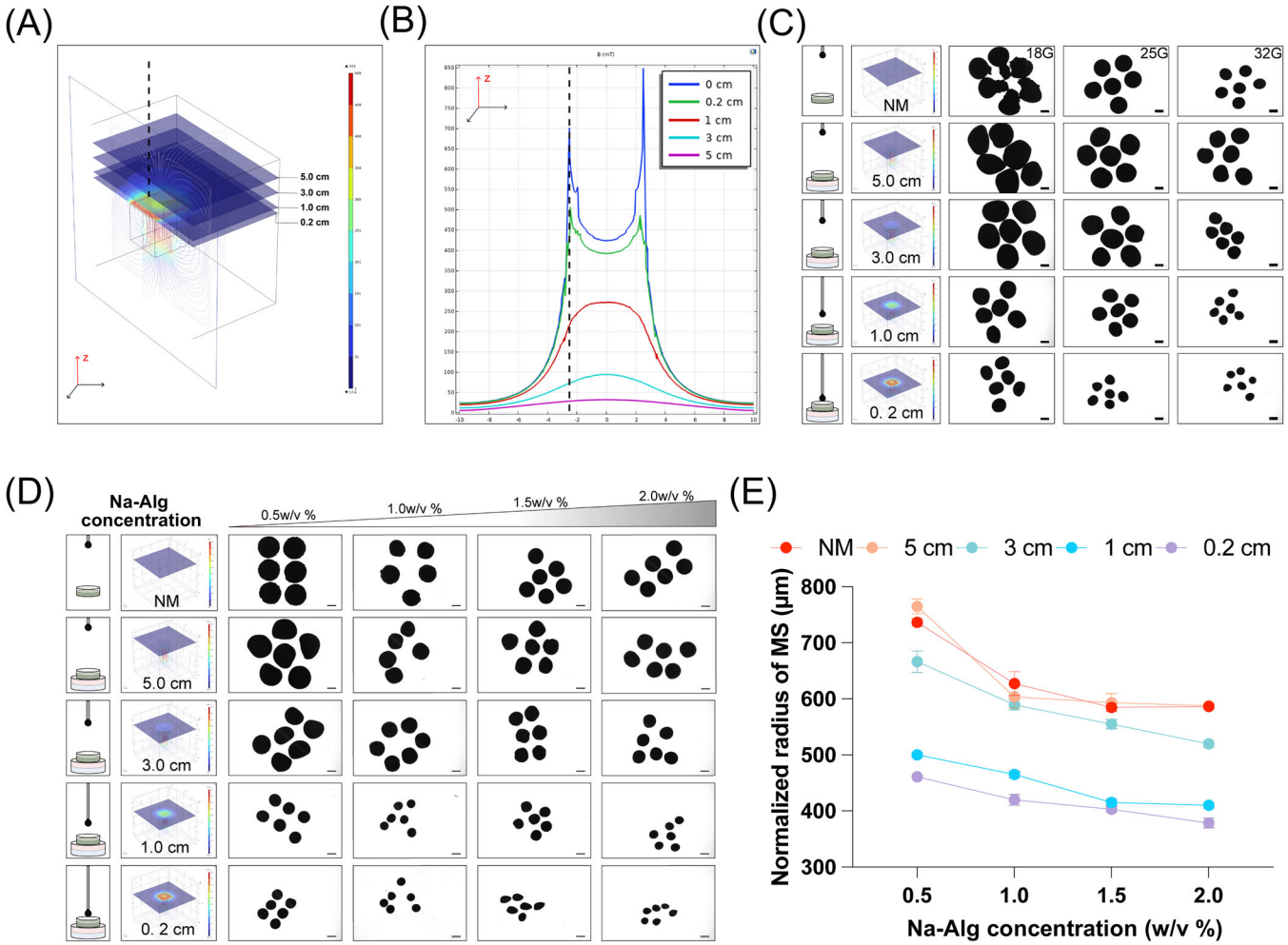

FIGURE 4 | Magnetic field distribution and fabrication of size-tunable microparticles. (A) Finite-element simulation of spatial magnetic flux distribution around a block-shaped NdFeB magnet, illustrating the *xy* plane at $z = 0.2$, 1, 3, and 5 cm. The color gradient (red to blue) represents the magnetic field intensity. The black-dashed line denotes the *Z*-axis direction. (B) Quantitative representation of the magnetic field intensity along the $y = -2.5$ cm plane for the four layers shown in (A). The curves depict the magnetic field intensity on each *xy* plane layer at different *Y*-axis positions, with the black-dashed line indicating the *Z*-axis direction. (C) Schematic, simulation, and experimental images demonstrate that the size of the microgels decreases as the distance to the magnetic field reduces, independent of nozzle size limitations. The color in the simulation images reflects changes in magnetic field intensity, scale bars: 400 μm. (D) Microscopic images of microgels with size modulated by varying Na-Alg concentrations, scale bars: 400 μm. (E) Statistical analysis of the normalized radius of microspheres at different Na-Alg concentrations and heights (MS, microspheres; NM, no magnet).

The magnetic-field-driven system enables precise control of droplet size by varying the magnet-nozzle distance, thereby validating the critical radius scaling law. Reducing the separation distance (z) significantly decreases droplet size, achieving a 50% volume reduction at $z = 0.2$ cm compared to gravity-only systems (Figure 4C), which is consistent with Supporting Information Derivation Formula. Nozzle diameter (D) influences detachment via surface tension (Equation 3), with gravity-only systems showing $R_{crit} \propto D^{1/3}$, confirmed experimentally (Figure S5A,B). Under magnetic actuation, a shift occurs at D = 360 μm (30 G nozzle), where smaller nozzles amplify magnetic control, transitioning from surface tension to magnetic-driven detachment (Figure S5C,D). These results highlight z and D as critical parameters for precisely tailoring microgel sizes (300–900 μm).

The material properties of the precursor solution significantly influence droplet dynamics beyond the control of the magnetic field. Contrary to the scaling law ($R_{crit} \propto \gamma^{\frac{1}{3}}$), increasing Na-Alg concentration (0.5 wt% to 2.0 wt%) under near-field magnetic conditions ($z = 0.2$–1 cm) unexpectedly reduced microgel diameters by 8–12% (Figure 4D,E). This deviation from theoretical predictions, detailed in Figure S6, stems from three mechanisms. First, low-concentration hydrogels spread at the interface before gelation due to weak viscoelastic resistance, allowing hydrodynamic collisions to dominate and expand the droplet footprint upon impact with the bath (Figure S6A). Second, SPIONs induce magneto-interfacial coupling, altering necking dynamics. Magnetic field gradients create anisotropic magnetostress, amplified by SPION crowding, which triggers non-classical fragmentation when the magnetostress surpasses viscoelastic recovery (Figure S6B). Third, Na-Alg concentration dictates SPION-polymer coupling efficiency (Figure S6C) [30]. Low concentrations permit SPION migration, causing heterogeneous stress and distorted interfaces, while high concentrations immobilize SPIONs via enhanced hydrogen bonding and entanglements, promoting uniform stress transfer. This explains

26924560, 2026, 5, Downloaded from https://onlinelibrary.wiley.com/doi/10.1002/agt2.70365 by Guosheng Tang - Nanjing Forestry University , Wiley Online Library on [20/05/2026]. See the Terms and Conditions (https://onlinelibrary.wiley.com/terms-and-conditions) on Wiley Online Library for rules of use; OA articles are governed by the applicable Creative Commons License

the paradoxical size reduction: higher viscosity resists capillary breakup, but reinforced networks accelerate necking through coherent magnetostress, deviating from Newtonian models.

To systematically characterize the formulation–property relationship, we further evaluated the mechanical properties of the spherical microgels by compression testing across a matrix of Na-Alg concentrations (1.0%, 1.5%, and 2.0%) and SPION loadings (2.5%, 5.0%, and 7.5%). Representative compressive stress–strain curves and the corresponding compressive modulus analysis indicate that increasing Na-Alg concentration consistently increases microgel stiffness (higher stress at a given strain and higher modulus), which is attributable to a denser polymer network and higher effective cross-link density (Figure S7). In addition, for each Na-Alg concentration, increasing SPION loading results in a monotonic increase in compressive modulus from 2.5% to 7.5%, suggesting a particle-reinforcement effect and/or additional physical constraints within the hydrogel matrix. Importantly, this mechanical tunability is achieved without altering the overall fabrication workflow, enabling application-oriented optimization by simultaneously tuning microgel size and stiffness.

Incorporating SPIONs allows precise control of microgel dimensions under magnetic actuation. Experiments showed a clear inverse relationship between SPION concentration (C) and microgel radius (R) in actuated systems, with no significant size change in gravity-only systems (non-magnetic controls, $p > 0.05$) (Figure S8A,B). This effect stems from the magnetic force ($F_B \propto \chi \nabla H^2$, Equation 2), where higher C boosts magnetic susceptibility, amplifying F_B and reducing the critical radius (R_{crit}) as derived in Supporting Information Derivation Formula. Scanning electron microscopy (SEM) confirmed dense SPION clustering at the microgel edge for $C > 2.5\%$ (Figure S8C). To further verify the edge-localized SPION enrichment observed at high SPION loading, we performed additional EDS elemental mapping on microgels prepared with 7.5% SPIONs. As shown in Figure S9, the microgel periphery exhibits dense particulate features in SEM, and the corresponding EDS maps reveal a strong Fe signal that spatially co-localizes with these clustered domains, confirming pronounced SPION enrichment at the microgel edge. Semiquantitative EDS analysis of the highlighted edge region indicates a high Fe fraction (56.95%), further supporting substantial peripheral accumulation of SPIONs under high-loading conditions.

Under magnetic actuation, microgel radii followed an unusual order: $R_{45°} < R_{90°} < R_{0°} < R_{NM} < R_{30°} < R_{60°}$, differing from classical pendant drop models. At 45°, the magnetic force aligns with gravity, thereby reducing surface tension resistance ($F_{\gamma,vertical} = \pi D\gamma \sin\theta$, Equation 2) and minimizing R_{crit}. Vertical (90°) and horizontal (0°) setups increased R_{crit} due to less effective force balance, while 30° and 60° angles caused uneven droplet breakup, enhancing adhesion and delaying detachment (Figure S10).

A fluorosilane-based superhydrophobic coating on the nozzle inner wall reduced R_{crit} by $10 \pm 3\%$ compared to untreated surfaces ($p < 0.001$), matching the theoretical scaling $R_{crit} \propto \gamma^{1/3}$ (Eq. S9). The coating minimized droplet adhesion, allowing detachment before static equilibrium (Figure S11). The bath calcium ion concentration (Ca^{2+}) had no significant effect on size. Near the magnet, rapid Na-Alg gelation prevented the formation of spherical shapes, leaving microgels with an initial droplet-like form (Figure S12). These results underscore the importance of SPIONs, magnet angle, and surface properties as key factors in controlling the size of microgels.

2.4 | Fabrication of Anisotropic Spherical Microgels and Fibrous Microgels

The magnetic actuation strategy enables rapid fabrication of homogeneous microgels and anisotropic microcarriers by controlling droplet interactions. Unlike traditional microfluidic or coaxial nozzle systems, this approach uses a novel platform where magnetic droplets collide and merge with non-magnetic droplets to form anisotropic microgels (Figure 5A). The platform enables precise temporal and spatial control over droplet fusion, allowing for the adjustment of structural anisotropy by tuning magnetic forces (Figure 5B). Magnetic droplets descend at controlled speeds and intercept non-magnetic precursor droplets from a lower nozzle to initiate compartmentalized fusion (Figure 5C). By modulating initial drop speed and flow rate ratios between the two nozzles, the platform tailors the magnetic and non-magnetic portions and shapes of the microgels (Figure 5D). These Janus composite droplets cross-link in a solution bath, maintaining magnetic alignment to form microgels with sharp interfacial boundaries between distinct material phases (Figure 5E).

Field-free operation highlights significant limitations: magnetically tagged upper droplets maintain spatial accuracy during impact; however, the resulting microgels form polydisperse aggregates with rough surfaces and fragmented internal structures (Figure S13A,B). This is due to insufficient kinetic energy transfer during collisions and dominant interfacial tension at the bath interface, leading to partial droplet flotation and asymmetric spreading. Conversely, applying a magnetization gradient force enhances impact energy, while vertical magnetic gradients facilitate complete droplet immersion and axisymmetric spreading through continuous actuation (Figure S13C). These magnetofluidic interventions produce monodisperse microgels with spherical morphology and distinct magnetic/non-magnetic boundaries, confirming magnetic control over assembly dynamics and solidification thermodynamics.

Leveraging the established magnetic microgel fabrication platform, a programmable shift from spherical microgels to continuous fibrous structures was achieved by adjusting extrusion parameters and applying a magnetic field. As shown in Figure 6A, varying the initial extrusion velocity (5–20 mL/h) drove a morphological transition from discrete magnetic microspheres (MagMS) to transient droplets, bead-on-a-string intermediates, and continuous fibrous microgels. Higher extrusion velocities increased shear rates within the nozzle, promoting shear-thinning behavior that reduced viscosity and facilitated continuous flow. Simultaneously, the hydrogel's viscoelastic properties ($G' > G''$) enable elastic recovery post-extrusion, countering capillary-driven Rayleigh–Plateau instabilities and stabilizing emerging filaments. Rapid ionic cross-linking then locked the elongated morphology, ensuring structural integrity and mechanical continuity.

The application of external magnetic fields enables fiber formation under conditions where passive extrusion fails to overcome

26924560, 2026, 5, Downloaded from https://onlinelibrary.wiley.com/doi/10.1002/agt2.70365 by Guosheng Tang - Nanjing Forestry University , Wiley Online Library on [20/05/2026]. See the Terms and Conditions (https://onlinelibrary.wiley.com/terms-and-conditions) on Wiley Online Library for rules of use; OA articles are governed by the applicable Creative Commons License

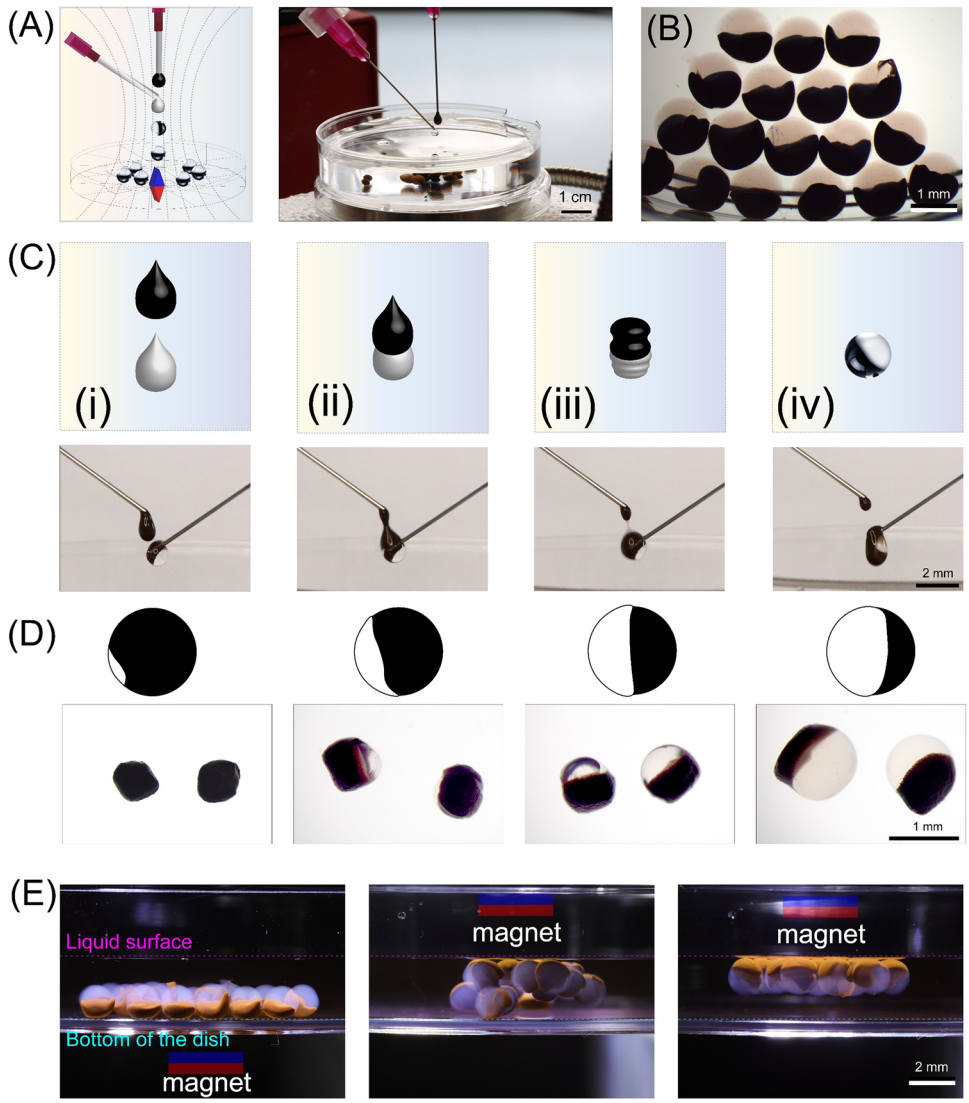

FIGURE 5 | Fabrication of anisotropic microgels with magnetic-field-driven. (A) Schematic and optical image illustration of anisotropic microsphere formation via magnetic-field-guided droplet fusion, showing the resultant anisotropic microgels, scale bars: 1 cm. (B) Optical image of anisotropic microspheres fabricated by magnetic-field-driven, scale bars: 1 mm. (C) Schematic and optical image illustration of time-resolved fusion dynamics: (i) pre-contact droplet alignment, (ii) initial interfacial contact, (iii) magnetic stress-induced directional merging with downward extrusion, and (iv) post-fusion microgel descent under continuous magnetic guidance, scale bars: 2 mm. (D) Schematic and optical image of structurally asymmetric Janus microgels with continuous tunability by adjusting hydrogel extrusion speeds, scale bars: 1 mm. (E) Optical image of field-directed alignment, rotational aggregation, and buoyancy-controlled levitation in liquid media, scale bars: 2 mm.

interfacial instabilities. As shown in Figure S13D,E, in the absence of magnetic intervention, viscous and elastic stresses are insufficient to counteract surface tension-driven droplet breakup; by contrast, directional magnetic fields stabilize continuous fiber production. The magneto-rheological effect regulates fiber architecture through magnetically induced alignment, counteracting interfacial relaxation and enabling control over morphology in discontinuous extrusion regimes. This magneto-alignment enhances the kinetics of fiber formation and dimensional precision. Magnetic fields produce uniform microgel fibers (Figure 6D) compared to irregular aggregates in field-free conditions (Figure 6B). Fiber diameter is finely tuned by nozzle gauge, achieving micrometer-scale precision (Figure 6C). These fibers exhibit spoolable continuity and mechanical robustness for coiling (Figure 6E), surpassing the mechanical properties of conventional discontinuous extrusion. Embedded superparamagnetic nanoparticles retain field-responsive mobility (Figure 6F), integrating process control and material functionality and mitigating the traditional trade-offs between fabrication speed and structural complexity.

2.5 | Field-Driven Microrobotic Motion and Pattern Assembly

The motion of magnetic microgels under external fields is governed by the interplay between applied magnetic fields and their intrinsic superparamagnetic properties. As illustrated in Figure 7A, the force decomposition on a single microgel revealed three key components: the radial force F_r, the axial force F_{Bz}, and

26924560, 2026, 5, Downloaded from https://onlinelibrary.wiley.com/doi/10.1002/agt2.70365 by Guosheng Tang - Nanjing Forestry University , Wiley Online Library on [20/05/2026]. See the Terms and Conditions (https://onlinelibrary.wiley.com/terms-and-conditions) on Wiley Online Library for rules of use; OA articles are governed by the applicable Creative Commons License

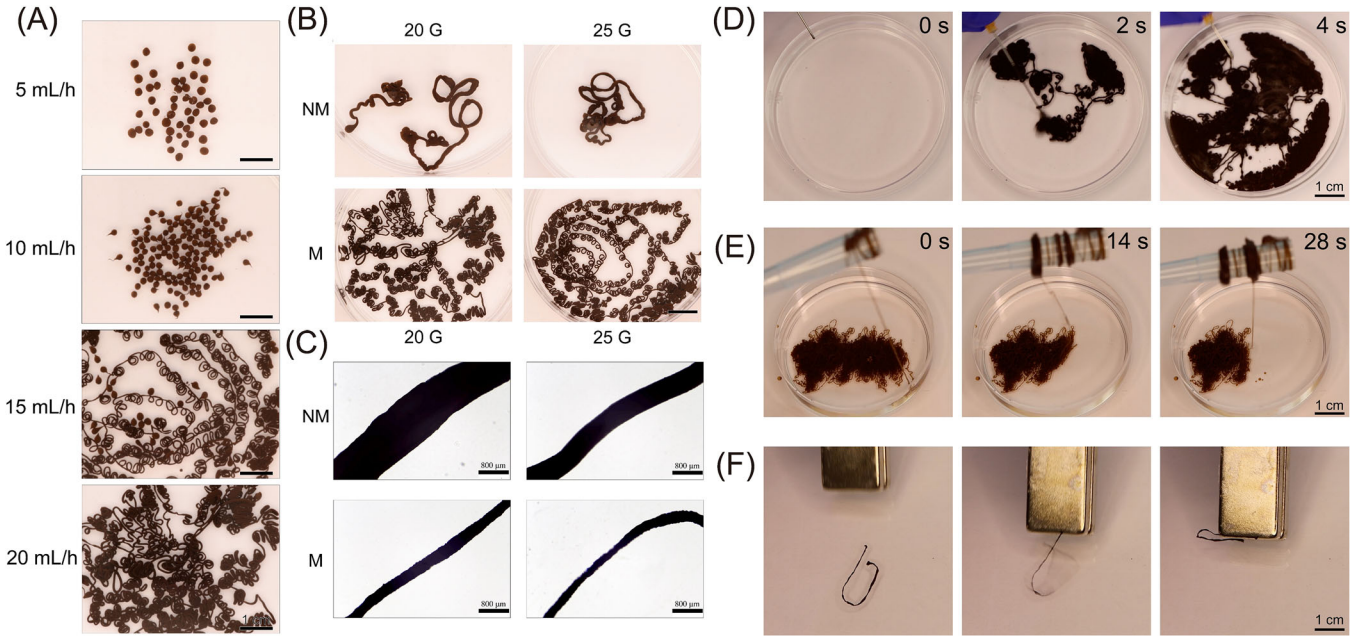

FIGURE 6 | Fabrication of fibrous microgel via magnetic-field-driven. (A) Optical image showing extrusion velocity-dependent morphology evolution (5–20 mL/h), transitioning from discrete microspheres to continuous microfibers governed by viscoelastic flow criteria, scale bars: 1 cm. (B) Optical image demonstrating nozzle gauge and magnetic field co-regulation of microfiber diameter (M, with magnet; NM, no magnet), scale bars: 1 cm. (C) Microscopic image of local region of microfibers (M, with magnet; NM, no magnet), scale bars: 800 μm. (D) Optical image showing the high-throughput microfiber production captured at 0–4 s, scale bars: 1 cm. (E) Optical image illustrating the spooling of microfibers, demonstrating their high degree of continuity, scale bars: 1 cm. (F) Optical image showing preserved magnetic-field-driven capability in microfibers, enabling potential shape reconfiguration, scale bars: 1 cm.

the transverse force F_{Bx}, all arising from the induced magnetization M in response to the applied field H_a. These forces collectively enabled both translational and rotational actuation, with the balance between F_{Bx} and F_{Bz} determining the directionality of motion along the field gradient.

To demonstrate spatiotemporal control, we fabricated a 5 × 5 cm micro-maze using SLA 3D printing (Figure 7B), whose geometry imposes precise constraints on particle trajectories. When a permanent magnet was positioned beneath the maze, the microgel exhibited rapid, field-guided navigation, completing the maze in approximately 10 s (Figure 7C and Video S3). Frame-by-frame analysis of the trajectory reveals a mean translational speed of about 0.5 cm/s, with near-zero deviation from the magnet's induced field gradient, which quantitatively indicates indicator of high directional fidelity.

Beyond linear translation, the microgels exhibit rich rotational dynamics under dynamic fields, as schematically depicted in Figure 7D. For a single microgel (i), the angle θ between the induced magnetization M and the applied field H_a governs its rotational response; when $\theta \neq 0$, a torque $\tau = m \times H_a$ drives reorientation. This mechanism enables in situ rotation (Figure 7E), where a single microgel completes a full 360° turn under about 1 s under a rotating field, as quantified from video tracking (Video S4). For two interacting microgels (ii), the induced dipoles align via magnetic attraction, resulting in synchronized orbital motion around their common center of mass (Figure 7F), with an orbital radius of about 500 μm and a period of 2 s. Extending to multi-particle systems (iii–iv), the collective behavior emerges as concentric rotational patterns (Figure 7G and Video S5), where particle density and field strength modulate the radius and angular velocity, a phenomenon we quantify as the rotational frequency scaling linearly with the applied field amplitude.

The programmable nature of this motion extends to macroscopic pattern assembly. Under spatially varying magnetic potentials, microgels self-organize into predefined architectural configurations (Figure 7H and Video S6). The assembly efficiency, defined as the fraction of particles correctly positioned within the boundary of the target pattern, reached 92% under optimized field parameters. At larger scales, these responsive traits persist: microgel fibers (Figure 7I) exhibit comparable motility, with individual segments executing coordinated bending and extension under field gradients, suggesting scalability for constructing hierarchical micro-mechanical systems.

Collectively, these results demonstrate that magnetic microgels combine high mobility, programmable assembly, and robust scalability—attributes essential for applications in targeted drug delivery, microvascular navigation, and bio-inspired robotics.

2.6 | Biocompatibility of Magnetic Alginate Microspherical Microgels

Due to the remarkable magnetic responsiveness of superparamagnetic microgels and their potential applications in biomedical

26924560, 2026, 5, Downloaded from https://onlinelibrary.wiley.com/doi/10.1002/agt2.70365 by Guosheng Tang - Nanjing Forestry University , Wiley Online Library on [20/05/2026]. See the Terms and Conditions (https://onlinelibrary.wiley.com/terms-and-conditions) on Wiley Online Library for rules of use; OA articles are governed by the applicable Creative Commons License

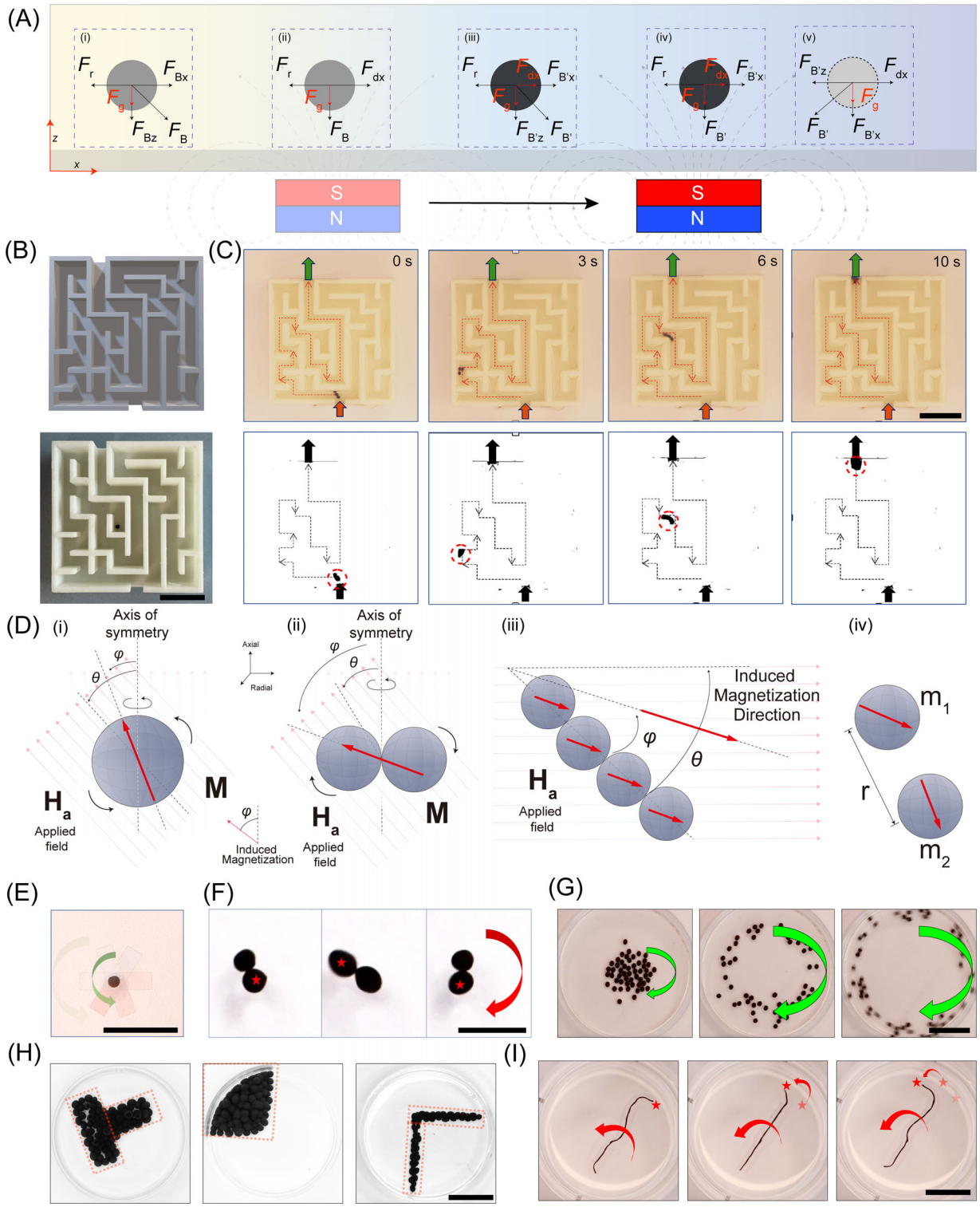

FIGURE 7 | Field-controlled dynamics and structural programming of superparamagnetic microgels. (A) Schematic of phase-resolved force analysis of magnetic navigation, illustrating key forces: F_B (magnetic force), F_r (fluid resistance), and F_g (gravitational force). (i) Initial contact with magnetic field; (ii) alignment under magnetic force; (iii) transient displacement lag during rapid field relocation; (iv) stabilization at new field position; and (v) magnetic locking suppressing inertial overshoot. (B) SLA-3D-printed micro-maze, scale bar: 15 mm. (C) Three microgels (black-dashed trajectories) following programmed magnetic guidance (red-dashed path) through maze channels within 10 s, scale bar: 15 mm. (D) Schematic illustrations of magnetization mechanisms under an applied magnetic field. Key symbols denote: M, magnetization vector (red arrows); H_a, applied magnetic field (gray-dashed arrow); φ, azimuthal angle between M and H_a; θ, polar angle between M (or H_a) and the axis of symmetry. (i) Single particle magnetization misalignment; (ii) dipole-coupled particle pair rotation; (iii) chain formation enabling collective torque; and (iv) non-contact magnetostatic interactions between dipoles. (E) In situ spinning of single microgel, scale bar: 10 mm. (F) Synchronized orbital motion of paired particles, scale bar: 10 mm. (G) Hierarchical concentric rotation of particle assemblies, scale bar: 10 mm. (H) The magnetic-field-directed in situ patterning of microgels, scale bar: 20 mm. (I) Magnetically responsive microfibers, scale bar: 20 mm.

26924560, 2026, 5, Downloaded from https://onlinelibrary.wiley.com/doi/10.1002/agt2.70365 by Guosheng Tang - Nanjing Forestry University , Wiley Online Library on [20/05/2026]. See the Terms and Conditions (https://onlinelibrary.wiley.com/terms-and-conditions) on Wiley Online Library for rules of use; OA articles are governed by the applicable Creative Commons License

fields, such as targeted delivery and modulation of the cellular microenvironment, assessing their acute toxicity and long-term biocompatibility is crucial for clinical translation. This study rigorously evaluated the biosafety of superparamagnetic alginate microspheres (SPIONs-AlgMS) using longitudinal co-culture models with human mesenchymal stem cells (MSCs) and A549 lung carcinoma cells.

Fluorescence imaging confirmed sustained cell viability across all conditions, with SPIONs-AlgMS-treated cells showing no acute cytotoxicity (Figure 8A,B and Figures S14–S16). This biocompatibility was corroborated in A549 co-culture models, where SPIONs-AlgMS had no adverse impact on cell viability (Figure S17). Non-magnetic AlgMS controls exhibited stable Calcein-AM fluorescence over 7 days, matching blank controls and verifying the Alg matrix's safety. Longitudinal analysis showed minimal dead cell accumulation in SPIONs-AlgMS groups, even during extended co-culture (Figure 8A,B), demonstrating that SPIONs-AlgMS maintain cellular homeostasis across various nanoparticle concentrations.

To further assess biocompatibility, human umbilical vein endothelial cells (HUVECs) were co-cultured with SPIONs-AlgMS to examine effects on vascular cell phenotype. Immunofluorescence analysis showed that CD31 expression and localization, a vital marker of endothelial junctional integrity and function, remained unaffected across all SPIONs-AlgMS concentrations and time points (Figure 8C and Figure S18). Semiquantitative analysis further confirmed no significant change in relative CD31 expression among all groups at Day 1, Day 4, and Day 7 (Figure 8E and Figure S18). This preserved CD31 expression confirms that superparamagnetic microgels do not impair essential adhesive or signaling properties of endothelial cells. To further assess endothelial cell–cell junction integrity, we additionally stained VE-cadherin, another key adherens junction marker, which exhibited comparable junctional localization across all SPIONs-AlgMS concentrations (Figure 8D and Figure S19) and no significant differences in semiquantified expression at Day 1, Day 4, and Day 7 (Figure 8F and Figure S19). In addition, tight-junction marker ZO-1 staining further showed intact junctional patterns over time with no apparent disruption following exposure to SPIONs-AlgMS (Figure S20). As a functional validation, a wound-healing (scratch) assay further confirmed that HUVEC migration (gap closure over 48 h) was not significantly affected by AlgMS or SPIONs-AlgMS across different SPION loadings (Figure S21). Together with viability data from MSCs and A549 cells, these results demonstrate that SPIONs-AlgMS sustain both cellular viability and critical functional traits across diverse cell types relevant to therapeutic applications.

To further evaluate blood compatibility, a hemolysis assay was performed to assess the potential erythrocyte membrane damage induced by SPIONs-AlgMS. Anticoagulated whole blood was incubated with SPIONs-AlgMS at the tested concentrations, using isotonic buffer and deionized (DI) water as negative and positive controls, respectively. The results showed low hemolytic activity of SPIONs-AlgMS under the tested conditions, indicating good hemocompatibility and suggesting that the microgels do not induce appreciable red blood cell membrane disruption (Figure S22).

2.7 | Application of Spherical Microgels as an Embolization Model

The potential of magnetically responsive microgels for vascular embolization was investigated using a physiologically relevant flow-controlled model. A Tesla valve structure, fabricated via SLA 3D printing with white resin, featured adjustable lumen diameters (1–10 mm) to mimic clinically relevant vascular sizes from arterioles to medium vessels (Figure 9A). The valve's asymmetric geometry, with inherent unidirectional conductivity, replicates the hemodynamic environment of branching vasculature by restricting reverse flow through branched conduits while allowing forward flow in the main channel (Figure 9B). Unlike conventional bidirectional flow systems, this biomimetic design provides an ideal platform for assessing embolization dynamics under controlled conditions.

In clinical practice, embolization stability is typically achieved using particulate embolics (e.g., polymer/hydrogel microspheres) for distal vessel packing, liquid embolics for cohesive cast formation, or device-based embolics such as coils for proximal occlusion [31]. These established agents are generally designed for durable residence at the target site. Compared with conventional non-magnetic microspheres that rely primarily on flow-driven lodging and particle packing for retention [32], our superparamagnetic microgels introduce an additional magnetic retention mechanism (field-induced aggregation and localization), which can enhance site-specific stability under flowing conditions in this in vitro model. As shown in Figure 9C, the embolization process began with magnetic induction-driven aggregation of superparamagnetic microspheres at specific sites within the Tesla valve. These microgels exhibited consistent retention efficacy across lumen diameters ranging from 1 to 10 mm, with robust dipole interactions under diverse geometric constraints. A localized magnetic field gradient enabled precise control over microgel accumulation, mimicking catheter-directed targeting used in clinical embolization.

Sequential imaging (Figure 9D) documented the shift from initial laminar flow in the main channel to progressive microgel deposition, resulting in complete rerouting of the flow. The magnetically stabilized embolus withstood elevated perfusion pressures, mimicking physiological stress, without dispersion of the microgel (Video S7). This stability stems from the interplay of magnetic microgel aggregation and the Tesla valve's flow-control mechanism. Superparamagnetic microspheres create shear-resistant networks at targeted sites, while the valve's asymmetric design passively prevents retrograde flow through secondary branches, simulating vascular collateralization. Importantly, under the current experimental conditions, the aggregate was formed and stabilized primarily during magnetic actuation. Although the Tesla valve geometry may also provide local hydrodynamic confinement, we did not independently quantify the long-term stability of the aggregate after removal of the magnetic field.

2.8 | Magnetically Enhanced Hemodialysis via Microgel Turbulence

To showcase the capabilities of magnetic microgels, their potential to improve hemodialysis efficiency through controlled

26924560, 2026, 5, Downloaded from https://onlinelibrary.wiley.com/doi/10.1002/agt2.70365 by Guosheng Tang - Nanjing Forestry University , Wiley Online Library on [20/05/2026]. See the Terms and Conditions (https://onlinelibrary.wiley.com/terms-and-conditions) on Wiley Online Library for rules of use; OA articles are governed by the applicable Creative Commons License

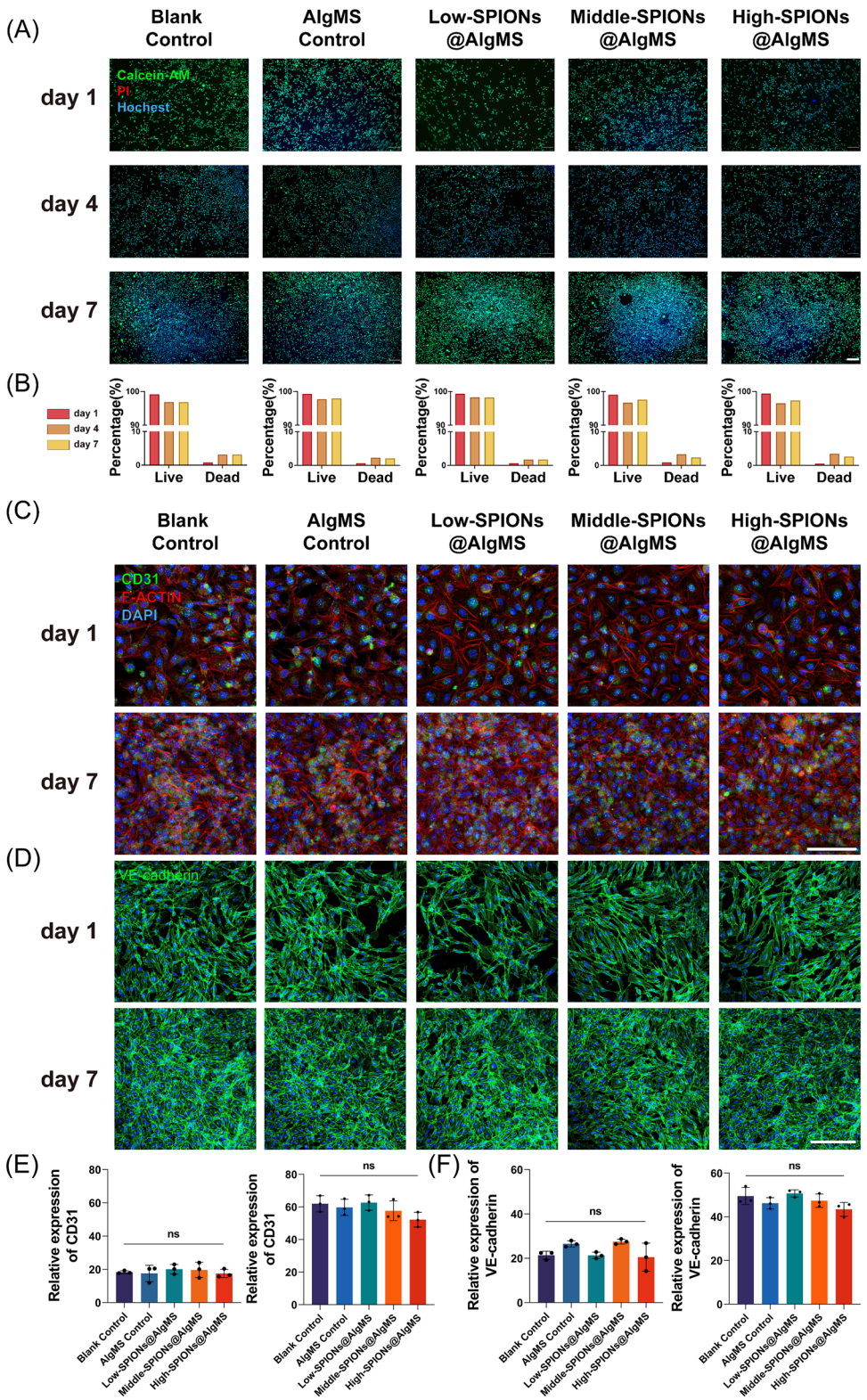

FIGURE 8 | Sustained viability and preserved function in cells co-cultured with superparamagnetic microgels. (A) Representative live/dead fluorescence microscopy images showing Calcein-AM (green, viable cells) and propidium iodide (PI, red, dead cells) staining for untreated control groups and SPIONs@AlgMS-treated groups at Days 1, 4, and 7 of co-culture with MSCs, scale bar: 400 μm. (B) Quantification of the live/dead cell ratio. (C) Immunofluorescence staining of HUVECs co-cultured with AlgMS or SPIONs-AlgMS showing CD31 (green), F-actin (red), and nuclei (DAPI, blue) at Days 1 and 7, scale bar: 400 μm. (D) Immunofluorescence staining of HUVECs showing VE-cadherin (green) and nuclei (DAPI, blue) at Days 1 and 7, scale bar: 200 μm. (E) Semiquantitative analysis of relative CD31 expression based on fluorescence intensity measurements at Days 1 and 7. (F) Semiquantitative analysis of relative VE-cadherin expression based on fluorescence intensity measurements at Days 1 and 7.

26924560, 2026, 5, Downloaded from https://onlinelibrary.wiley.com/doi/10.1002/agt2.70365 by Guosheng Tang - Nanjing Forestry University , Wiley Online Library on [20/05/2026]. See the Terms and Conditions (https://onlinelibrary.wiley.com/terms-and-conditions) on Wiley Online Library for rules of use; OA articles are governed by the applicable Creative Commons License

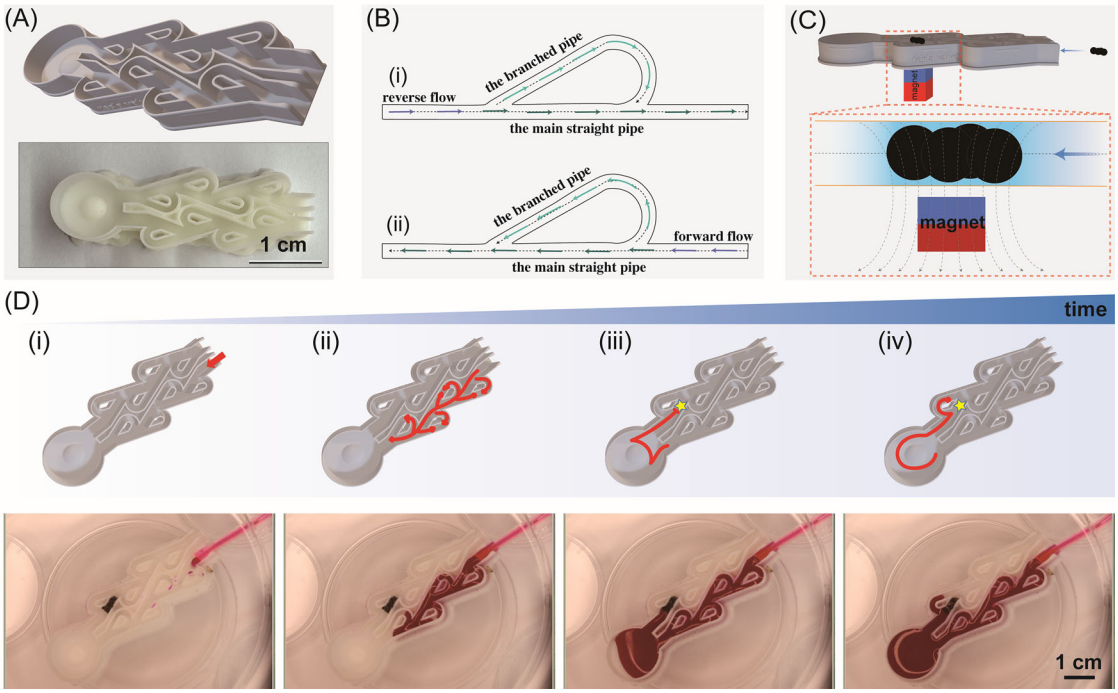

FIGURE 9 | Biomimetic embolization simulation using a Tesla valve model. (A) Top: STL digital model of the Tesla valve; Bottom: 3D-printed physical prototype in white resin, replicating the STL design with high surface fidelity, scale bar: 2 cm. (B) Directional flow resistance mechanism: (i) reverse flow encounters elevated resistance through branched pipes and (ii) forward flow preferentially traverses the main straight channel. (C) Magnetic-field-guided aggregation of microspheres (black clusters) at target sites, with magnet positioning indicated. (D) Temporal evolution of post-embolization fluid dynamics: (i–iv) Sequential snapshots showing progressive occlusion of the main channel and subsequent redirection of flow into secondary branched pathways. Upper panels: Theoretical fluid trajectories through the embolized Tesla valve at successive time points. Lower panels: Experimentally observed flow patterns under perfusion, demonstrating collateral flow rerouting and complete channel blockage. Scale bar: 1 cm.

hydrodynamic manipulation was investigated. Hemodialysis employs extracorporeal circulation, using peristaltic pumps and heparin anticoagulation to pass blood through a dialyzer. Countercurrent diffusion and ultrafiltration between blood and a dialysate of purified water and electrolytes remove metabolic wastes, such as urea, uric acid, creatinine, and small-molecular toxins (Figure 10A). Despite advances, prolonged treatment times (4–6 h/session) remain due to limitations in passive solute transport across dialysis membranes.

For hemodialysis, clearance efficiency is governed by the overall mass-transfer resistance across the dialyzer, which includes membrane transport as well as boundary-layer (film) resistances on the blood- and dialysate-sides. Therefore, conventional clinical/engineering strategies typically improve solute clearance by optimizing dialyzer structure and hydrodynamics (e.g., hollow-fiber geometry, flow distribution, and dialysate-side mass-transfer enhancement), rather than altering the membrane separation mechanism itself [33, 34]. Against this backdrop, our magnetically driven microgels should be viewed as an active, field-controlled transport enhancement element. By inducing controllable micro-scale turbulence, the microgels can disrupt concentration polarization and reduce the effective boundary-layer resistance near the membrane surface, thereby increasing the driving force for diffusive transport and improving apparent clearance. Specifically, magnetic torque-induced rotation created localized turbulent flows (Reynolds number: 50–200), disrupting stagnant boundary layers and boosting convective mass transfer (Figure 10B). To examine operational stability under prolonged actuation, the microgels were subjected to continuous magnetic stimulation for 24 h and imaged at representative time points (Figure S23). The microgels maintained a stable spherical morphology throughout the 24 h stimulation without visible fragmentation or collapse, supporting their robustness under extended magnetic manipulation. Moreover, to further assess the potential leakage risk of SPIONs under dialysis-relevant conditions, we quantitatively measured Fe ion release from SPIONs-loaded microgels into the surrounding medium (Figure S24). The Fe ion concentration in the external medium remained at a safe low level throughout the test period, indicating negligible Fe leaching under the evaluated dialysis-related conditions.

Experiments compared conventional alginate microspheres (AlgMS), static MagMS, and magnetically actuated groups (AlgMS + Mag Field, MagMS + Mag Field). After 6 h of dialysis, magnetic rotation groups showed significant clearance improvements in urea (3.1×), uric acid (4.0×), and creatinine (2.6×) compared to non-actuated controls ($p < 0.01$). Remarkably, magnetically driven dialysis achieved equivalent toxin removal to standard 6-h protocols in just 3 h, cutting treatment time by 50% (Figure 10C). SPIONs-loaded Alg microgels demonstrated selective copper ion (Cu^{2+}) adsorption through surface chelation, achieving 32% Cu^{2+} clearance compared to standard dialysis (Figure 10C). In Alg-based microgels, Cu^{2+} capture is widely attributed to coordination/chelation between Cu^{2+} and the carboxylate groups (—COO^-) along alginate chains, accompanied by ion-exchange with pre-existing cross-linking cations. In this binding mode, Cu^{2+} is immobilized via inner-sphere complexation/

26924560, 2026, 5, Downloaded from https://onlinelibrary.wiley.com/doi/10.1002/agt2.70365 by Guosheng Tang - Nanjing Forestry University , Wiley Online Library on [20/05/2026]. See the Terms and Conditions (https://onlinelibrary.wiley.com/terms-and-conditions) on Wiley Online Library for rules of use; OA articles are governed by the applicable Creative Commons License

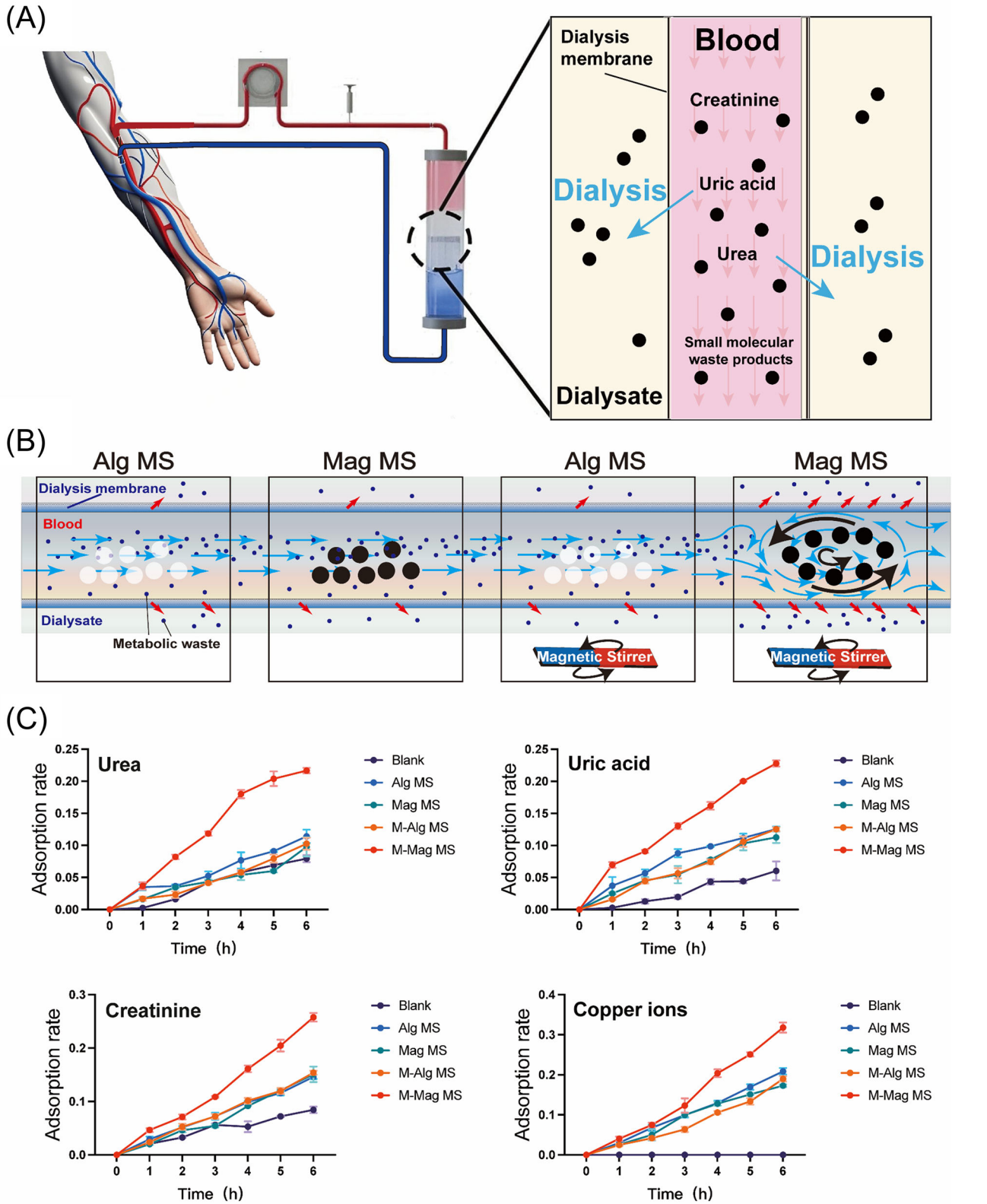

FIGURE 10 | Magnetically augmented hemodialysis platform. (A) Schematic of dialysis circuit: blood and dialysate counterflow through the dialyzer, enabling waste exchange (urea, uric acid, creatinine). (B) Schematic of experimental groups. Under a magnetic field, MagMS (black spheres) rotates within the dialyzer's fluidic channel, generating microscale vortical flows (blue spirals). (C) Time-dependent clearance kinetics of urea, uric acid, creatinine, and copper ion across experimental groups. Data represent mean ± SD ($n = 3$).

26924560, 2026, 5, Downloaded from https://onlinelibrary.wiley.com/doi/10.1002/agt2.70365 by Guosheng Tang - Nanjing Forestry University , Wiley Online Library on [20/05/2026]. See the Terms and Conditions (https://onlinelibrary.wiley.com/terms-and-conditions) on Wiley Online Library for rules of use; OA articles are governed by the applicable Creative Commons License

ionic cross-linking rather than weak physical adsorption, which is consistent with previous reports that alginate-derived sorbents often follow pseudo-second-order kinetic behavior (chemisorption-dominant uptake) and can be described by Langmuir-type adsorption at equilibrium [35, 36]. This dual capability—simultaneous toxin removal and heavy metal adsorption—makes the system a promising therapeutic platform for hypercupremia, where conventional dialysis is less effective. The microgels retained their structural stability, supporting their suitability for continuous-flow clinical applications.

3 | Conclusion and Discussion

This study presents an innovative magnetic-field-driven approach for microgel fabrication, utilizing internal stress gradients from SPIONs embedded in hydrogel precursors to achieve self-segmentation without the need for external shear forces or physical templates. By modulating magnetic flux density and extrusion dynamics, the method enables contactless, programmable control over microgel architectures, allowing for the on-demand generation of diverse architectures—from uniform spherical microgels to anisotropic Janus particles and fibrous microgel assemblies. The SPIONs-driven magnetomotive self-segmentation employs field-programmable body forces to destabilize precursor interfaces, yielding tunable particle sizes (300–900 μm) and high-throughput production while maintaining payload integrity. The multifunctionality of SPION-loaded microgels was demonstrated in two clinically relevant scenarios. In vascular embolization, magnetically guided aggregation within a biomimetic Tesla valve system enabled scalable occlusion across a range of vessel sizes (1–10 mm), integrating active magnetic retention with passive hydrodynamic stabilization. In hemodialysis, magnetically induced microgel rotation creates localized turbulence, boosting the clearance of urea, uric acid, and creatinine, while also facilitating selective copper ion adsorption—a dual capability not achieved by conventional dialysis. These findings highlight magnetic microgels as versatile platforms for biomedical engineering applications.

To further position this magnetic-driven strategy within the broader landscape of microgel manufacturing technologies, we briefly compare it with commonly used preparation routes and discuss its potential translational complementarity. For example, microgels are also widely prepared via free-radical polymerization routes (e.g., precipitation/emulsion polymerization) and emulsion-templated methods, which can be efficient and scalable but often involve radical initiators and/or surfactants and require additional purification or demulsification steps to remove residual small molecules, oils, and surfactants—potentially increasing the processing burden for biomedical translation, especially when sensitive biological payloads are involved. In parallel, microfluidic microgel fabrication technologies have shown strong translational potential by enabling standardized production of monodisperse, cargo- or cell-laden microgels for biomedical uses such as diagnosis, disease monitoring, drug screening, and therapeutic delivery, including emerging clinical-oriented implementations [37]. Building on this translational context, our chip-free, all-aqueous magnetic-driven strategy is positioned to complement microfluidic routes by offering a simplified and scalable alternative when rapid bulk production, reduced device complexity, and shear-free processing are desired for practical deployment and manufacturing.

From the perspective of embolization-related applications, the present work should be regarded primarily as a proof-of-concept demonstration of magnetically assisted embolization behavior. Compared with representative embolization microrobots and microswarms reported previously, which mainly emphasize stable swarm formation [38], post-aggregation adhesion/stabilization [39], or precise embolization in complex vascular environments [40], the main emphasis of the present work is on establishing a shear-free, all-aqueous, and microfluidics-free magnetic fabrication strategy for multifunctional hydrogel microgels. More importantly, this strategy provides a versatile platform for the functional design of microgels, enabling magnetic guidance, controllable assembly, and localized embolization behavior under external magnetic fields.

At the same time, the embolization experiments performed in the SLA-printed Tesla valve should be interpreted within the scope of an in vitro model. Although this platform provides a controllable and reproducible branching-like geometry for visualizing magnetically guided aggregation, retention, and flow rerouting, it remains a simplified analog of the vascular environment. In particular, the rigid resin structure does not recapitulate vascular compliance or elasticity, and the applied flow conditions cannot fully reproduce the non-Newtonian rheology of blood or the contributions of cellular and tissue components. Therefore, the current results mainly support magnetically assisted embolization behavior under field actuation, while the long-term stability of the aggregates after removal of the magnetic field still requires further investigation. Future work will further evaluate these behaviors using more physiologically relevant models, such as ex vivo perfused vessels and vascular organ-on-a-chip systems, which better incorporate multicellular architecture, extracellular matrix, and defined mechanical stimuli [37].

Beyond the structural and hemodynamic limitations of the current in vitro model, successful clinical translation will also depend on a more comprehensive understanding of the biological responses to these magnetic microgels in vivo. While in vitro biosafety has been established, the in vivo microenvironment, including immune interactions, clearance pathways, and long-term material fate, requires systematic investigation. For clinical translation, long-term SPION retention and biodistribution must be rigorously evaluated to prevent nanoparticle-mediated systemic toxicity. In parallel with these safety evaluations, future development should integrate biodegradable SPIONs with soft robotic microgels, enabling stimuli-responsive navigation and precision targeting through programmable shape morphing and motility. This synergistic approach, combining advanced materials and clinical knowledge, will yield adaptive microsystems capable of intelligent and minimally invasive interventions.

To realize the potential of such adaptive and intelligent microsystems, the logical next step is to advance from qualitative demonstration to predictive quantitative control. The magnetomotively driven behaviors described in this work, including self-segmentation, guided aggregation, and induced rotation, are fundamentally governed by microscale forces and torques. This study has successfully established its functional outcomes.

26924560, 2026, 5, Downloaded from https://onlinelibrary.wiley.com/doi/10.1002/agt2.70365 by Guosheng Tang - Nanjing Forestry University , Wiley Online Library on [20/05/2026]. See the Terms and Conditions (https://onlinelibrary.wiley.com/terms-and-conditions) on Wiley Online Library for rules of use; OA articles are governed by the applicable Creative Commons License

However, the precise quantification of key kinematic parameters, such as actuation speed and magnetic torque, and the rigorous establishment of their correlation with the applied magnetic field strength, are essential for engineering reliable closed-loop control. Subsequent work employing techniques like high-speed microrheology and calibrated magnetic tweezers will be necessary to define these quantitative force–motion relationships. Transforming the current proof of concept into a predictive design platform in this manner will pave the way for the programmable shape morphing, navigation, and precision targeting required in the next generation of minimally invasive biomedical microrobots.

4 | Experimental

4.1 | Materials and Fabrication

SPIONs (Fe_3O_4) were purchased from Macklin (CAS: 1317-61-9). The nominal particle size provided by the supplier is 20 nm, and the nanoparticles were used as received without additional surface modification. Na-Alg (SA, 0.5–2.5 wt%) and SPIONs (1–20 wt%) were dispersed in DI water via ultrasonication. The homogeneous SA/SPIONs solution was magnetically stirred (500 rpm, 2 h) to ensure uniformity. The precursor solution was extruded through nozzles (20–34 gauge) using a microfluidic syringe pump (New ERA, 0.1–1000 μL/min) into a $CaCl_2$ coagulation bath (2–10 wt%, DI water). Magnetic-field-driven was achieved via an N52-grade neodymium block (50 × 50 × 25 mm^3, residual magnetism > 1.2 T) or cylindrical magnet (Ø 50 × 25 mm, residual magnetism > 1.2 T) mounted on a 3-axis translational stage. Fabricated microgels were rinsed thrice with DI water to remove excess Ca^{2+}. Key equipment included a fluorescence microscope (MSHOT MF53-N), scanning electron microscope (JEOL JSM-7800F), compression system (TA.XT plus C, SMS, Britain), and syringe pumps.

4.2 | Microgel Formation Protocol

The SA/SPIONs composite solution was extruded through a nozzle positioned 0.2–5 cm above the magnetic field source. Under controlled flow rates (1–50 mL/h), droplets were generated and guided by magnetic forces into the $CaCl_2$ bath, resulting in instantaneous ionic cross-linking to form spherical or magnetically deformed microgels (Figure 1D). Magnetic actuation experiments were performed using permanent NdFeB block magnets (N54 grade; Shanghai Jincheng Magnetic Material Co. Ltd.; dimensions: 50 × 50 × 50 mm). The magnetic flux density (B) at the sample/nozzle position was calibrated by direct measurement using a handheld Gaussmeter (Hirst GM08, calibrated). Unless otherwise stated, all reported magnetic field values correspond to the measured B at the sample location under the specified magnet–sample separation distance.

4.3 | Characterization and Measurements

Microgels were rinsed with DI water and re-suspended for analysis. Projected areas of hydrated microgels were quantified using ImageJ (NIH) from optical micrographs. For irregular shapes, theoretical areas were calculated via integral geometry. SEM examined morphological details. To correlate microgel behavior with external stimuli, magnetic field distributions were modeled using finite-element analysis software COMSOL Multiphysics.

4.4 | Biocompatibility Assessment

MSCs and A549 cells were co-cultured with microgels (10% SPIONs-SA) at low, medium, and high densities (10, 100, and 1000 particles/mm^2) for 1–4 days. Negative controls were treated with 75% ethanol for 5 min. Cell viability was assessed using a LIVE/DEAD Kit (Thermo Fisher), following the manufacturer's protocols. Fluorescent images (488/530 nm for live cells; 570/610 nm for dead cells) were acquired and quantified (MSHOT MF53-N).

4.5 | Magnetic Responsiveness and Functional Testing

Magnetic guidance: Microgels were navigated through a PDMS-sealed microfluidic maze (Formlabs SLA-printed resin) using an NdFeB magnet ($10 \times 10 \times 50$ mm^3) to simulate vascular embolism. Tesla valve mimicry: A 3D-printed Tesla valve (dye-stained DI water) evaluated directional flow resistance under a magnetic-field-driven condition. Dialysis acceleration: A custom dialysis system (SPIONs-loaded microgels) employed external magnetic stirrers (500 rpm) to enhance solute exchange rates.

4.6 | Adsorption of Metabolic Waste in Blood

The concentration of metabolic waste (creatinine, urea, and uric acid) in the plasma was measured by a chemiluminescence immune detection system (CL-6000i, Mindray, China). The experiment was conducted in a simulated vascular circulation system (CD0056, Chuangdao 3D Medical Technology, China) under controlled conditions (37°C, pH 7.4, with dynamic flow). At predetermined times (0, 1, 2, 3, 4, 5, 6 h), a plasma sample was withdrawn and centrifuged at 4000 rpm for 5 min, after which the 300 μL supernatant was added to the system.

$$\text{Adsorption rate} = \frac{c_0 - c_t}{c_0} \times 100\%$$

where C_0 is the initial concentration of metabolic waste, and C_t is the concentration of metabolic waste at time.

4.7 | Statistical Analysis

All experiments were performed in triplicate ($n \geq 3$ per group). Data are expressed as mean ± SD. Statistical significance ($p < 0.05$) was determined via one-way ANOVA with Tukey's post hoc test (GraphPad Prism 9.0).

Author Contributions

Yingying Hou: investigation, visualization, writing – original draft. **Huaibin Wang:** data curation, formal analysis, writing – original draft. **Long Chen:** methodology, validation, writing – original draft. **Kangrui**

26924560, 2026, 5, Downloaded from https://onlinelibrary.wiley.com/doi/10.1002/agt2.70365 by Guosheng Tang - Nanjing Forestry University , Wiley Online Library on [20/05/2026]. See the Terms and Conditions (https://onlinelibrary.wiley.com/terms-and-conditions) on Wiley Online Library for rules of use; OA articles are governed by the applicable Creative Commons License

Yuan: methodology, validation. **Jianhua Qiu:** investigation, methodology. **Lijie Chen:** investigation. **Bingbing Zhan:** methodology. **Zeqing Li:** visualization. **Lingran Du:** visualization. **Maobin Xie:** writing – review and editing. **Zeyu Luo:** supervision, writing – review and editing. **Yongqing He:** formal analysis, supervision, writing – review and editing. **Guosheng Tang:** conceptualization, funding acquisition, supervision, writing – review and editing.

Acknowledgments

This work was supported by the National Natural Science Foundation of China (NSFC) Program (No. 32201183). We are especially grateful to Prof. Xiaolong Fan at the Key Laboratory of Magnetism and Magnetic Materials of the Ministry of Education, Lanzhou University, for his pivotal theoretical contributions, and to Dr. Monika Golda-Cepa for her enlightening discussions and intellectual inspiration throughout this work.

Conflicts of Interest

The authors declare no conflicts of interest.

References

1. L. Xuan, Y. Hou, L. Liang, et al., "Microgels for Cell Delivery in Tissue Engineering and Regenerative Medicine," *Nano-Micro Letters* 16 (2024): 218.

2. Z. Liu, J. Wu, Z. Luo, et al., "3D Biofabrication of Microporous Hydrogels for Tissue Engineering," *Advanced Healthcare Materials* 14 (2025): e2403583.

3. Y. Hou, L. Xuan, W. Mo, et al., "Anisotropic Microcarriers: Fabrication Strategies and Biomedical Applications," *Advanced Materials* 37 (2025): 2416862.

4. G. Tang, R. Xiong, D. Lv, et al., "Gas-Shearing Fabrication of Multicompartmental Microspheres: A One-Step and Oil-Free Approach," *Advanced Science* 6 (2019): 1802342.

5. T. Moragues, D. Arguijo, T. Beneyton, et al., "Droplet-Based Microfluidics," *Nature Reviews Methods Primers* 3 (2023): 32.

6. I. Yoon, A. Shum, and L. D. H. D. Weitz, "Fabrication of phospholipid vesicles from double emulsions in microfluidics," *Bulletin of the American Physical Society* 53, Abstract X8.00007, p. 50 (2008), http://meetings.aps.org/link/BAPS.2008.MAR.X8.7.

7. L.-Y. Chu, A. Utada, R. Shah, J. W. Kim, and D. Weitz, "Controllable Monodisperse Multiple Emulsions," *Angewandte Chemie International Edition* 46 (2007): 8970–8974.

8. H. Kim, D. Luo, D. Link, D. Weitz, M. Marquez, and Z. Cheng, "Controlled Production of Emulsion Drops Using an Electric Field in a Flow-Focusing Microfluidic Device," *Applied Physics Letters* 91 (2007): 133106.

9. Q. Feng, D. Li, Q. Li, X. Cao, and H. Dong, "Microgel Assembly: Fabrication, Characteristics and Application in Tissue Engineering and Regenerative Medicine," *Bioactive Materials* 9 (2022): 105.

10. Q. Feng, D. Li, Q. Li, et al., "Assembling Microgels via Dynamic Cross-Linking Reaction Improves Printability, Microporosity, Tissue-Adhesion, and Self-Healing of Microgel Bioink for Extrusion Bioprinting," *ACS Applied Materials & Interfaces* 14 (2022): 15653.

11. Z. Chen, Z. Lv, Z. Zhang, et al., "Advanced Microfluidic Devices for Fabricating Multi-Structural Hydrogel Microsphere," *Exploration* 1 (2021): 20210036.

12. Y. Xu, H. Zhu, A. Denduluri, et al., "Recent Advances in Microgels: From Biomolecules to Functionality," *Small* 18 (2022): 2200180.

13. S. Deng, W. Shang, S. Feng, et al., "Controlled Droplet Transport to Target on a High Adhesion Surface With Multi-Gradients," *Scientific Reports* 7 (2017): 45687.

14. L. Wu, Z. Dong, F. Li, and Y. Song, "Designing Laplace Pressure Pattern for Microdroplet Manipulation," *Langmuir* 34 (2018): 639.

15. M. C. Mendes, J. A. Pereira, A. S. Silva, and J. F. Mano, "Magneto-Enzymatic Microgels for Precise Hydrogel Sculpturing," *Advanced Materials* 36 (2024): 2402988.

16. B. Kong, R. Liu, J. Guo, L. Lu, Q. Zhou, and Y. Zhao, "Tailoring Micro/Nano-Fibers for Biomedical Applications," *Bioactive Materials* 19 (2023): 328–347.

17. C. Zhou, C. Wang, K. Xu, et al., "Hydrogel Platform With Tunable Stiffness Based on Magnetic Nanoparticles Cross-Linked GelMA for Cartilage Regeneration and Its Intrinsic Biomechanism," *Bioactive Materials* 25 (2023): 615–628.

18. S. Ganguly and S. Margel, "3D Printed Magnetic Polymer Composite Hydrogels for Hyperthermia and Magnetic Field Driven Structural Manipulation," *Progress in Polymer Science* 131 (2022): 101574.

19. E. M. Greeson, C. S. Madsen, A. V. Makela, and C. H. Contag, "Magnetothermal Control of Temperature-Sensitive Repressors in Superparamagnetic Iron Nanoparticle-Coated *Bacillus subtilis*," *ACS Nano* 16 (2022): 16699.

20. Z. Ding, Y. Cai, H. Sun, et al., "Janus Hydrogel Microrobots With Bioactive Ions for the Regeneration of Tendon-Bone Interface," *Nature Communications* 16 (2025): 2189.

21. H. Wang, Y. Hou, L. Chen, et al., "Superparamagnetic Hydrogels: Precision-Driven Platforms for Biomedicine, Robotics, and Environmental Remediation," *Biomedical Technology* 10 (2025): 100084.

22. X. He, Y. He, G. Wen, and F. Jiao, "Evolution and Breakup of a Ferrofluid Droplet Neck Through a Capillary Tube," *Chemical Engineering Science* 289 (2024): 119882.

23. R. E. Rosenweig, *Ferrohydrodynamics* (Cambridge University Press, 1985).

24. A. P. Stikuts, R. Perzynski, and A. Cēbers, "Small Deformation Theory for a Magnetic Droplet in a Rotating Field," *Physics of Fluids* 34 (2022): 052010.

25. K. Xu, C. P. Tostado, J.-H. Xu, Y.-C. Lu, and G.-S. Luo, "Direct Measurement of the Differential Pressure During Drop Formation in a Co-Flow Microfluidic Device," *Lab on a Chip* 14 (2014): 1357.

26. B. T. Helenbrook and C. F. Edwards, "Quasi-Steady Deformation and Drag of Uncontaminated Liquid Drops," *International Journal of Multiphase Flow* 28 (2002): 1631.

27. L. Shao, B. Pan, R. Hou, Y. Jin, and Y. Yao, "User-Friendly Microfluidic Manufacturing of Hydrogel Microspheres With Sharp Needle," *Biofabrication* 14 (2022): 025017.

28. W. J. Seeto, Y. Tian, S. Pradhan, P. Kerscher, and E. A. Lipke, "Rapid Production of Cell-Laden Microspheres Using a Flexible Microfluidic Encapsulation Platform," *Small* 15 (2019): 1902058.

29. C. Zhang, R. Grossier, L. Lacaria, F. Rico, N. Candoni, and S. Veesler, "A Microfluidic Method Generating Monodispersed Microparticles With Controllable Sizes and Mechanical Properties," *Chemical Engineering Science* 211 (2020): 115322.

30. K. Danas, S. V. Kankanala, and N. Triantafyllidis, "Experiments and Modeling of Iron-Particle-Filled Magnetorheological Elastomers," *Journal of the Mechanics and Physics of Solids* 60 (2012): 120–138.

31. D. Wang and W. Rao, "Bench-to-Bedside Development of Multifunctional Flexible Embolic Agents," *Theranostics* 13 (2023): 2114.

32. H. Wu, S. Lv, R. Zhang, et al., "Next-Generation Flexible Embolic Systems: Targeted Transarterial Chemoembolization Strategies for Hepatocellular Carcinoma," *Advanced Materials* 37 (2025): 2503971.

33. S. Yu, X. Yan, C. Wang, et al., "A Non-invasive, Closed-Loop Electronic Stent for Real-Time Management of Gastroesophageal Reflux Disease," *Advanced Fiber Materials* 8 (2026): 289–302.

34. J. Luo, J. B. Fan, and S. Wang, "Recent Progress of Microfluidic Devices for Hemodialysis," *Small* 16 (2020): 1904076.

26924560, 2026, 5, Downloaded from https://onlinelibrary.wiley.com/doi/10.1002/agt2.70365 by Guosheng Tang - Nanjing Forestry University , Wiley Online Library on [20/05/2026]. See the Terms and Conditions (https://onlinelibrary.wiley.com/terms-and-conditions) on Wiley Online Library for rules of use; OA articles are governed by the applicable Creative Commons License

35. H. Zhang, X. Han, J. Liu, et al., "Fabrication of Modified Alginate-Based Biocomposite Hydrogel Microspheres for Efficient Removal of Heavy Metal Ions From Water," *Colloids and Surfaces A: Physicochemical and Engineering Aspects* 651 (2022): 129736.

36. J. Zhao, H. Li, C. Mu, S. Zhang, F. Shi, and J. Hu, "Performance and Mechanism of L-Arginine Modified Alginate Aerogels for Adsorption of Cadmium and Copper Ions," *Journal of Polymers and the Environment* 32 (2024): 5086–5097.

37. D. S. Veliz, K. L. Lin, and C. Sahlgren, "Organ-on-a-Chip Technologies for Biomedical Research and Drug Development: A Focus on the Vasculature," *Smart Medicine* 2 (2023): e20220030.

38. J. Law, X. Wang, M. Luo, et al., "Microrobotic Swarms for Selective Embolization," *Science Advances* 8 (2022): eabm5752.

39. D. Jin, Q. Wang, K. F. Chan, et al., "Swarming Self-Adhesive Microgels Enabled Aneurysm on-Demand Embolization in Physiological Blood Flow," *Science Advances* 9 (2023): eadf9278.

40. X. Liu, L. Wang, Y. Xiang, et al., "Magnetic Soft Microfiberbots for Robotic Embolization," *Science Robotics* 9 (2024): eadh2479.

Supporting Information

Additional supporting information can be found online in the Supporting Information section.

Supporting File 1: agt270365-sup-0001-SuppMat.docx.

Supporting File 2: agt270365-sup-0002-VideoS.zip.

26924560, 2026, 5, Downloaded from https://onlinelibrary.wiley.com/doi/10.1002/agt2.70365 by Guosheng Tang - Nanjing Forestry University , Wiley Online Library on [20/05/2026]. See the Terms and Conditions (https://onlinelibrary.wiley.com/terms-and-conditions) on Wiley Online Library for rules of use; OA articles are governed by the applicable Creative Commons License